Variations of the North Pacific Subtropical Mode Water from Direct Observations

LUC RAINVILLE

Applied Physics Laboratory, University of Washington, Seattle, Washington

STEVEN R. JAYNE

Physical Oceanography Department, Woods Hole Oceanographic Institution, Woods Hole, Massachusetts

MEGHAN F. CRONIN

NOAA/Pacific Marine Environmental Laboratory, Seattle, Washington

(Manuscript received 10 April 2013, in final form 3 December 2013)

ABSTRACT

Mooring measurements from the Kuroshio Extension System Study (June 2004–June 2006) and from the ongoing Kuroshio Extension Observatory (June 2004–present) are combined with float measurements of the Argo network to study the variability of the North Pacific Subtropical Mode Water (STMW) across the entire gyre, on time scales from days, to seasons, to a decade. The top of the STMW follows a seasonal cycle, although observations reveal that it primarily varies in discrete steps associated with episodic wind events. The variations of the STMW bottom depth are tightly related to the sea surface height (SSH), reflecting mesoscale eddies and large-scale variations of the Kuroshio Extension and recirculation gyre systems. Using the observed relationship between SSH and STMW, gridded SSH products and in situ estimates from floats are used to construct weekly maps of STMW thickness, providing nonbiased estimates of STMW total volume, annual formation and erosion volumes, and seasonal and interannual variability for the past decade. Year-to-year variations are detected, particularly a significant decrease of STMW volume in 2007–10 primarily attributable to a smaller volume formed. Variability of the heat content in the mode water region is dominated by the seasonal cycle and mesoscale eddies; there is only a weak link to STMW on interannual time scales, and no long-term trends in heat content and STMW thickness between 2002 and 2011 are detected. Weak lagged correlations among air–sea fluxes, oceanic heat content, and STMW thickness are found when averaged over the northwestern Pacific recirculation gyre region.

1. Introduction

The North Pacific Subtropical Mode Water (STMW) is a thick layer of water with nearly uniform properties found south of the Kuroshio Extension (Masuzawa 1969; Hanawa and Talley 2001; Oka and Qiu 2012). To first order, the formation rates and properties of STMW are thought to be dependent on the wintertime atmospheric air–sea fluxes (Bingham 1992; Suga and Hanawa 1995), which are associated with synoptic weather patterns, in particular cold air outbreaks from the Asian continent (Konda et al. 2010). The surface mixed layer, in direct contact with the atmosphere, is typically only a few tens of meters deep over the warm season, but can reach 300–400 m in winter. During winter, cold, dry continental air blows across the warm Kuroshio Extension water, resulting in some of the largest net surface heat fluxes from the ocean to the atmosphere found in the entire North Pacific basin (Wyrtki 1965). In the spring, as the net surface heat flux changes sign (becoming a heat gain rather than heat loss by the ocean), a seasonal thermocline begins to form, effectively trapping the ventilated water, which creates a subsurface layer, 300–400-m thick, with little stratification and nearly uniform temperature ($T \approx 16°$–$19.5°$C), referred to as the STMW (Oka 2009).

To the extent that the STMW retains its properties, it provides a memory of its ventilated surface conditions. Thus, the next time the STMW is exposed to the

Corresponding author address: Luc Rainville, Applied Physics Laboratory, University of Washington, 1013 NE 40th St., Seattle, WA 98105.
E-mail: rainville@apl.washington.edu

DOI: 10.1175/JCLI-D-13-00227.1

atmosphere, this water from the previous ventilation event reemerges to again interact with the atmosphere (Alexander and Deser 1995). During the ventilation events, the mixed layer can be several hundred meters thick, damping the sea surface temperature changes. Heat lost to the atmosphere tends to also be replenished through heat advection by the warm currents (Vivier et al. 1999, 2002; Cronin et al. 2013). As a consequence, the upper ocean not only responds to the air–sea heat fluxes, but can also potentially sustain or even change these fluxes. Based upon 15 yr (1993–2008) of sea surface height (SSH; a proxy for heat content) and latent and sensible heat losses estimated from numerical weather prediction product reanalyses, Kelly et al. (2010) found a weak correlation in the Gulf Stream whereby flux anomalies lagged heat content by 3 months. A similarly signed correlation was found in the Kuroshio Extension, although it was not statistically significant. Moreover, Bond and Cronin (2008) showed that on interannual time scales, the cold season heat flux anomalies in the Kuroshio Extension region were not related to change in the occurrence of regional weather patterns, suggesting that the ocean may be a driving factor.

Despite the fact that the western North Pacific is a relatively well sampled region of the world oceans, observations of STMW are still sparse in time and space. Scattered observations and ship transects need to be heavily averaged to offer a consistent picture of the STMW distribution, particularly because of the strongly meandering Kuroshio and large eddies often present in the area (Suga and Hanawa 1995). Processes governing the evolution of the STMW are still debated. Some studies suggest that the formation is a localized process and that the STMW rapidly spreads out over the entire gyre by horizontal advection (Suga and Hanawa 1995). On the other hand, it has been suggested that STMW in the recirculation gyre is isolated and all the decay in the thickness observed over the course of the year is attributable to local vertical mixing (Qiu et al. 2006). By studying STMW generation and erosion in a high-resolution model (Parallel Ocean Program model), Rainville et al. (2007) found that advection (particularly eddy transport) is critical, but enhanced vertical mixing is necessary to locally erode the STMW during the winter. On shorter time scales, processes that can enhance dissipation, such as near-inertial internal wave breaking and trapping by eddies or mean currents, might play an important role in eroding STMW. The variability of the volume of STMW present in a high-resolution model [Estimating the Circulation and Climate of the Ocean, Phase II (ECCO2)], and its relationship to the atmospheric forcing and climate variability, have been further explored by Davis et al. (2011).

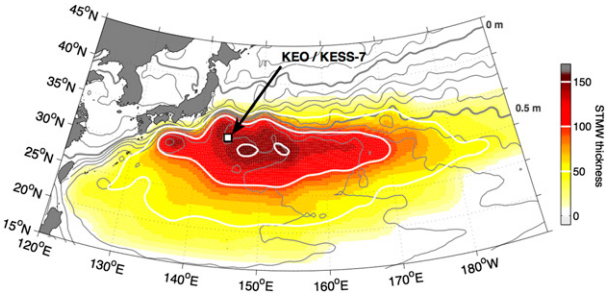

FIG. 1. Mean mode water thickness from floats using all profiles collected between 2001 and 2010. White contours are plotted at 50-m thickness intervals. Mean SSH contours (Maximenko et al. 2009) are plotted in gray (0.1-m intervals, with the 0- and 0.5-m contours thickened). The location of the KEO/KESS-7 moorings is indicated.

This paper presents direct observations of STMW collected from a subsurface profiling mooring deployed during the Kuroshio Extension System Study (KESS) observational period, between 2004 and 2006, and from a nearby surface mooring, the Kuroshio Extension Observatory (KEO), located in the southern recirculation gyre of the Kuroshio Extension since 2004 (Cronin et al. 2008). Complementary to the high vertical resolution of the KESS mooring and the long, high temporal resolution of the KEO mooring, the Argo float program (supplemented during KESS) provides 101 334 profiles in the western North Pacific (5°–50°N, 120°E–180°) from the beginning of 2002 to the end of 2011, from which STMW thickness can be derived (Fig. 1). In each float profile, the STMW layer is identified as the water that satisfies $16° < T < 20°\text{C}$ and $Q < 2 \times 10^{-10}\,\text{m}^{-1}\,\text{s}^{-1}$. STMW is detected in a little more than 30 000 float profiles during these 10 yr. The average thickness map shown in Fig. 1 is obtained from objective maps assuming a Gaussian covariance with a decorrelation scale of about 300 km (see section 4).

Our approach combines the direct observations from the moorings and floats with satellite data to explore the properties and variability of the STMW over the last 10 yr. The details of the float and mooring data are presented in section 2. The variability of the STMW around the KEO/KESS-7 mooring site is discussed in section 3, particularly in terms of processes involving seasonal variability, gyre-scale variability, mesoscale eddies, and finescale motions (specifically inertial internal waves). Maps of STMW and upper ocean heat content are built in section 4 and are used to estimate the total volume of STMW and how much is formed and eroded each year across the entire western North Pacific and in the southern recirculation gyre of the Kuroshio Extension. A discussion of the variability of STMW and

heat content on seasonal and longer time scales, and how they relate to air–sea heat fluxes (section 5), is followed by a summary of the results (section 6).

2. Observations

a. KESS-7 mooring

With the goal of better understanding the processes that govern intense meandering, eddy variability, recirculation gyres, and STMW associated with the Kuroshio Extension, the KESS moored array was deployed in summer 2004 and recovered in summer 2006 (Donohue et al. 2008). The array was centered on the first quasi-stationary meander crest and trough east of Japan, which is also the region of highest eddy kinetic energy. KESS observations included subsurface moorings, profiling floats, inverted echosounders with pressure and current meters, and a surface mooring (KEO). The KESS subsurface moorings were initially deployed in June 2004, then turned around in June 2005, and finally recovered in June 2006. The subsurface moorings, equipped with upward-looking acoustic Doppler current profilers (ADCPs; sampling from 25 to 250 m), McLane moored profilers (MPs), and a few deep current meters, resolve the fluctuations in the density and velocity fields throughout the water column for time scales from hourly to seasonal over the observational period. The MPs provided temperature, salinity, and velocity measurements between 250 and 1500 m every 15 h.

In this paper, we discuss data from the southernmost KESS subsurface moorings (KESS 7), located near the KEO surface mooring. The two moorings are always within 15 km. This site is in the region where the STMW is historically thickest (Fig. 1). At KESS 7, the deep temperature sensors, current meters, and ADCPs (30–250 m) yielded almost complete time series. The MPs at KESS 7 suffered some mechanical failures (failing after 8 and 9.5 months in the first and second years of the field program, respectively), but the overall data return, defined as the probability that a data point is present in any given 1-m depth bin of the set profiling range and any given day during the 2-yr deployment, is 65%. Schematics of the moorings are shown in Fig. 2.

b. KEO mooring

The KEO mooring, a slack-line, surface mooring maintained by the National Oceanic and Atmospheric Administration/Pacific Marine Environmental Laboratory (NOAA/PMEL), is anchored at about 32°20′N, 144°30′E. KEO carries a suite of meteorological sensors to measure winds, air temperature, relative humidity, rainfall, and solar and longwave radiation as well as

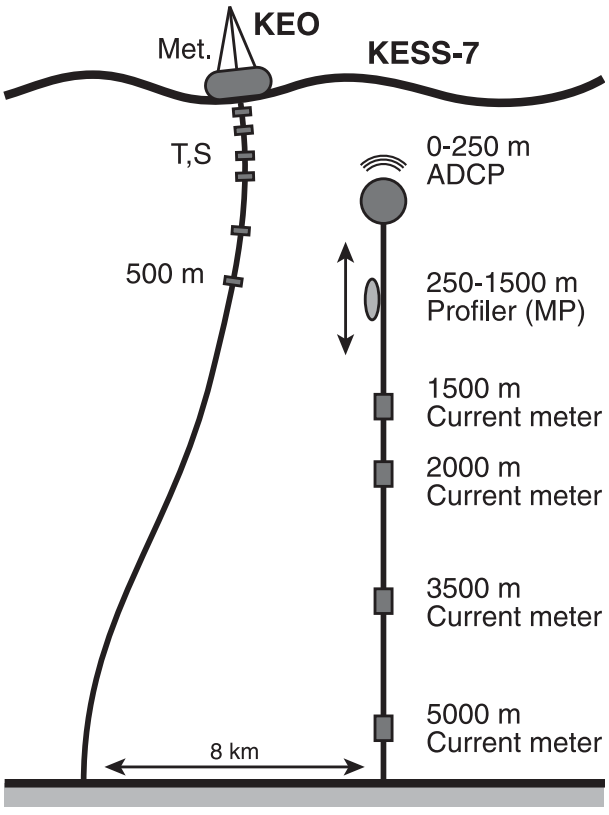

FIG. 2. Schematic of the KEO surface and KESS subsurface moorings. The KEO mooring is a slack-line mooring, with a watch circle of 6 km, anchored 8 km away from the subsurface KESS-7 mooring. The number of subsurface instruments on KEO is greater than shown.

subsurface sensors to monitor upper ocean temperature, salinity, and currents in the upper 500 m. KEO measured temperature at 12 depths and salinity at 9 depths between 1 and 500 m during its first KESS deployment. More sensors were added in the following years. The depths of the sensors are determined from the measured pressure of the sensor or interpolated from nearby pressure sensors. The KEO surface mooring has a watch circle radius of about 6 km and was anchored about 8 km from KESS 7. The KEO mooring was first deployed in June 2004 and is an ongoing OceanSITES time series reference station (Cronin et al. 2008).

Data from the subsurface and surface moorings are combined to obtain the time series of temperature and potential vorticity Q (defined here from the potential density gradient alone, as in Talley 1988) at the KESS-7 mooring shown in Fig. 3. The approximate 200-m thick layer with temperature around 16°–20°C and low potential vorticity ($Q < 2 \times 10^{-10}\,\mathrm{m^{-1}\,s^{-1}}$), particularly obvious in 2004 and 2005, is defined as the STMW. Using the well-resolved KESS data, we find that for waters with a

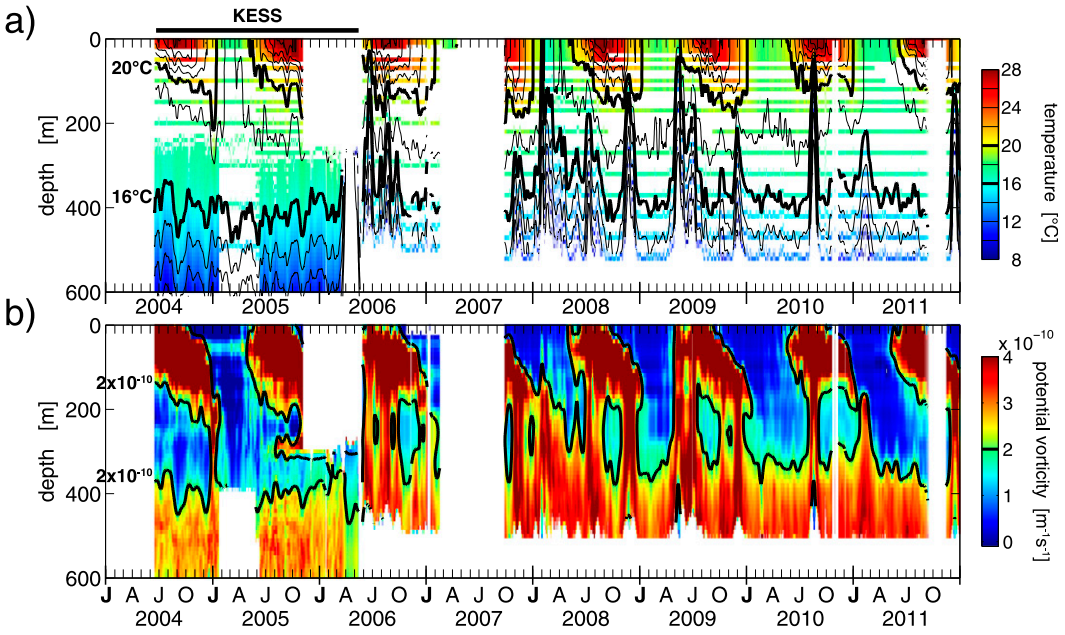

FIG. 3. Depth–time map of (a) measured temperature, contoured with 0.2°C intervals (the 16° and 20°C contours are thickened) and (b) vertically interpolated potential vorticity at the KEO site, with the addition of the KESS-7 mooring data during the KESS period (June 2004–June 2006). After June 2006, the potential vorticity is estimated from temperature gradient alone; $Q = 2 \times 10^{-10}\,\mathrm{m^{-1}\,s^{-1}}$ is denoted by the thickened contour.

range of temperatures and salinities typical of the STMW, the potential vorticity condition ($Q < 2 \times 10^{-10}\,\mathrm{m^{-1}\,s^{-1}}$) corresponds to a vertical temperature gradient smaller than $0.015°\mathrm{C\,m^{-1}}$ (Hanawa and Talley 2001). Using this condition, we extend the estimate of the STMW top and bottom depth (and thickness) past June 2006 to the entire KEO deployment (Fig. 3b), a period when the vertical resolution is good for temperature but generally weak for salinity.

Seasonal cooling and deepening of the surface mixed layer, seen as the low-Q water at the surface, is evident in each fall, reaching maximum depth in February or March of each year and penetrating to the STMW layer (to depths over 300 m). This is generally followed by the formation of a seasonal thermocline resulting from warming at the surface in April and restratification of the upper 200 m of the water column, isolating the STMW from the atmosphere. Large interannual trends are also obvious: STMW mostly disappears (or is broken up) between early 2006 and 2009. Variability also happens on shorter time scales.

c. Sea surface height

The SSH used in this analysis is the merged satellite altimetry gridded sea level product from the Archiving, Validation, and Interpretation of Satellite Oceanographic data (AVISO) collaboration (Ducet et al. 2000). The SSH, or absolute dynamical topography, is obtained by adding the AVISO mapped SSH anomalies to the 1992–2002 ocean mean dynamic topography (MDT) derived by Maximenko et al. (2009). Note that here we use a different MDT than Qiu et al. (2006) and Cronin et al. (2013). The MDT from Maximenko et al. (2009) is chosen as being most representative of the mean circulation in the Kuroshio Extension based on operational experience during the KESS cruises and previous studies (Rio and Hernandez 2004; Maximenko et al. 2009).

d. Floats

The global profiling float array provides the greater spatial and temporal context for the mooring measurements. To enhance the Argo global array, the KESS collaboration deployed 48 profiling floats in the Kuroshio Extension and its recirculation gyres, which provided a detailed description of the temporal evolution of the temperature and salinity structures in the upper water column. In the Kuroshio Extension, the number of float profiles increased by a factor of 4 during the KESS observational period (Table 1). Since then, the float network has been roughly stable, with over 12 000 profiles per year in the western North Pacific. The data from that enhanced float array in the Kuroshio Extension during 2004–06 has been discussed by Qiu et al. (2006, 2007a) and Jayne et al. (2009). Here we expand on their analysis to explore the mechanisms responsible for the variability of the properties of the STMW, both on shorter time

TABLE 1. Number of good floats profile from 2002 to 2011 in the western North Pacific (WP: 5°–50°N, 120°E–180°), in the RG (28°–35°N, 140°–150°E), and in the geographical region of the RG and with SSH > 0.75 m, for each year considered in this study. Profiles are deemed good if they extend from the near-surface (minimum pressure less than 50 dbar) to pressures over 500 dbar (1 dbar = 100 hPa). Increases in the number of profiles because of the addition of the KESS floats are highlighted in boldface.

Year	2002	2003	2004	2005	2006	2007	2008	2009	2010	2011
Profiles in WP	3245	4160	5585	8925	12 496	13 473	14 189	12 986	12 151	14 124
Profiles in RG	373	225	**878**	**1246**	890	917	550	706	587	713
Profiles in RG and with SSH > 0.75 m	335	163	**849**	**1123**	692	785	420	569	529	598

scales near KEO/KESS-7 mooring and seasonal and multiyear time scales over the entire gyre, by accounting for potential sampling biases in the float network distribution.

In the Kuroshio Extension, both the large-scale and mesoscale circulations play a significant role in controlling the distribution of the STMW (Uehara et al. 2003; Rainville et al. 2007). To exclude the cyclonic (cold core) eddies generated or propagating through the region, Qiu et al. (2007a) define the recirculation gyre as the area where the SSH is above a threshold value, greater than 2.0 m using the MDT of Teague et al. (1990), a condition that corresponds to SSH > 0.75 m with the MDT of Maximenko et al. (2009). In this study, we instead use a definition of the recirculation gyre (RG) strictly in terms of a geographical constraint (28°–35°N, 140°–150°E) and specify whether we impose the SSH constraint or not. Expanding Fig. 7 of Qiu et al. (2007a), the time series of temperature and potential vorticity from 2002 until 2011 in the recirculation gyre with the SSH constraint are shown in Figs. 4b and 4c. The locations of the 6063 profiles satisfying these conditions during the period considered are shown in Fig. 4a; 1022 profiles are in the geographical area but do not satisfy the SSH condition (~14%). A 7-day running mean has been applied to both the temperature and potential vorticity fields. Profiles meeting the geographic and SSH conditions and occurring on the same day are averaged together. To show the distribution of the data, no time interpolation is used in Fig. 4b, but small time gaps (less than 7 days) are filled using linear interpolation in Fig. 4c. Note the increased sampling associated with the deployments of the KESS floats in June 2004 and June 2005, almost all of which are in locations with SSH > 0.75 m.

Starting in 2005, the Kuroshio system became strongly meandering, resulting in more eddies and higher variability in the position of the jet (Qiu and Chen 2005; Donohue et al. 2008). This transition between the stable and unstable dynamical states strongly affected the dispersion of the floats. Many floats were captured by strong eddies and Kuroshio Extension meanders and ejected from the recirculation gyre, resulting in a sharp decrease in the number of profiles between 2005 and 2006, particularly those with the SSH condition.

The floats provide invaluable information about the spatial distribution of the STMW (Qiu et al. 2007a). However, because of its continuously variable distribution, the float array is susceptible to sampling biases. The time series of the average of the gridded SSH estimates (from AVISO) over the entire RG (28°–35°N, 140°–150°E) are shown in Fig. 5. The gridded satellite SSH is considered the true distribution of SSH, reflecting all the phenomena present in the region. Using the along-track SSH instead of the gridded product does not change the distributions (not shown). The primary signal is a seasonal variation, with a peak-to-peak amplitude of 0.20 m. Removing this seasonal average (obtained from binning data into their yearday and doing a 1-month running mean), the time series of SSH in the RG shows a small multiyear variation with a maximum range of 0.13 m (black line in Fig. 5b). The probability density functions of all the SSH estimates from the gridded product during two sets of years (2004–05 and 2009–10) are shown in Figs. 5b and 5d. For each float profile in the same region (28°–35°N, 140°–150°E) from 2002 to 2011, the SSH at the time and location of the profile is estimated by interpolating the AVISO gridded data in time and space (Fig. 5a). The same time data without the seasonal average are shown in Fig. 5b.

Particularly in the summers of 2004 and 2005, the floats preferably sampled high values of SSH because of the large number of floats released during KESS in the anticyclonic, southern RG. During the first year of KESS, there was little eddy activity and almost no variation in the position of the first Kuroshio meanders, and floats seeded in the RG stayed there. Very few floats sampled locations with small values of SSH. Starting in 2006, the large eddy kinetic energy dispersed the floats over the entire area, and the sampled probability density function is closer to that of the entire box region. In later years, it appears that the distribution of floats is slightly biased toward sampling a narrower distribution of SSH with not as many floats sampling high values of SSH, as floats have been found to preferably stay in cyclonic eddies and tend to be ejected from anticyclonic eddies

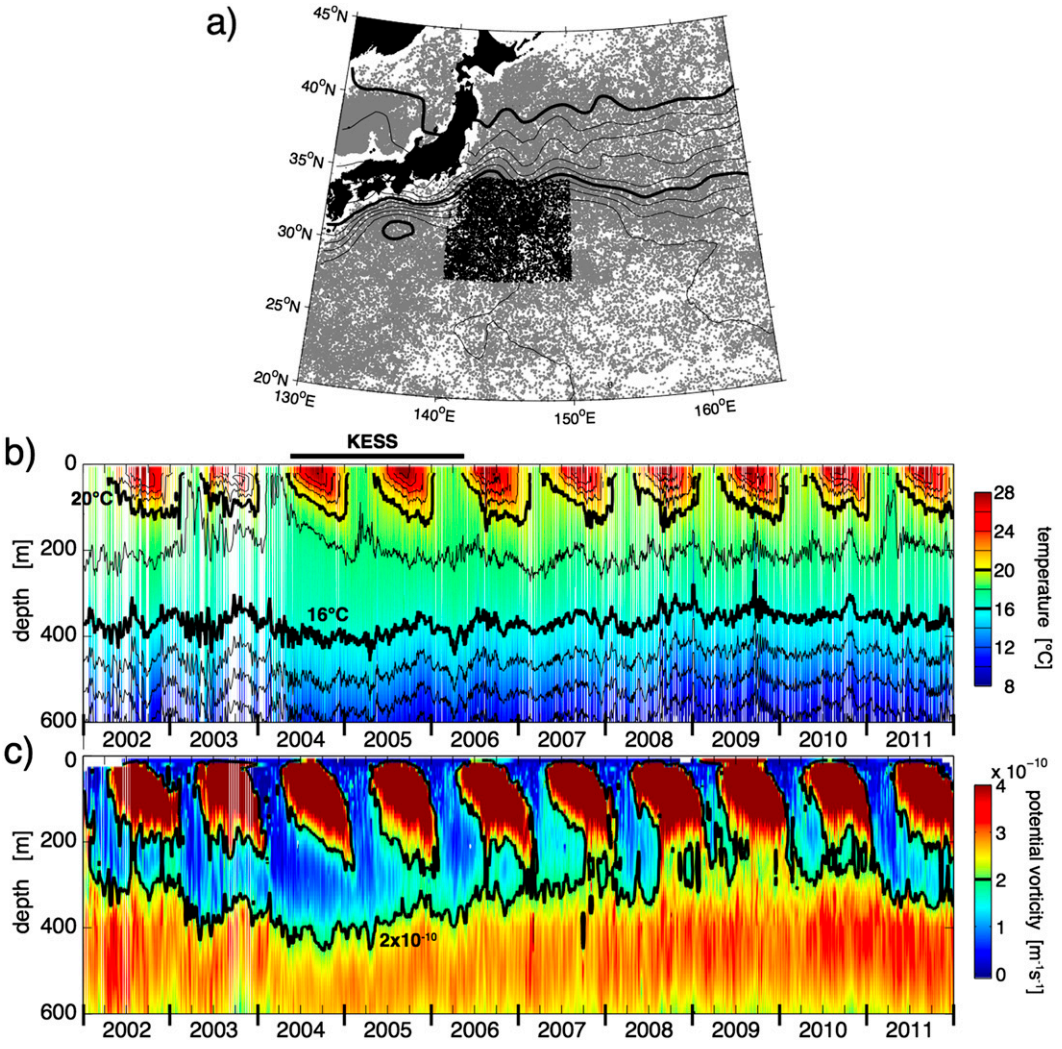

FIG. 4. (a) Location of all float profiles (in gray). Black dots represent the locations of the profiles satisfying the geographic and the SSH condition (>0.75 m) defining the recirculation gyre, from 2002 to the end of 2011. Mean SSH is also plotted (0.1-m interval and the contours at 0.5-m intervals are thickened). Depth–time maps in the recirculation gyre from floats of (b) temperature (only plotted when a profile exists on a given day), with isotherms contoured with 2°C intervals (16° and 20°C contours are thickened) and (c) interpolated potential vorticity (2×10^{-10} $m^{-1} s^{-1}$ contour is thickened). Gaps longer than 7 days are left blank in (c).

(Legg and McWilliams 2002). Figure 5 demonstrates that the float array is ever changing and that it is important to consider the profiles in their mesoscale context when averaging float data together.

3. STMW in the recirculation gyre

a. *Float and mooring time series*

The passage of several eddies is evident in the mooring data record (Fig. 3), which can be problematic if only mooring data are used. On the other hand, drifting floats (Fig. 4) do not sample the ocean uniformly. The vertical resolution is better for floats than for the moorings in the upper 200 m, but the strong temporal variations observed at the mooring site are smoothed out in the float record by the coarser temporal sampling scheme used by the floats and by the large spatial averaging that is used here. The aggregate of float data from the large region spanning different dynamical states might introduce some biases in our time series. Therefore, we argue that an approach combining the different data sets is required in order to understand both the temporal and vertical structure of the water mass.

As pointed out by Qiu et al. (2006), the seasonal evolution of the STMW is striking. Deep winter mixed layers penetrate to the STMW in February and March

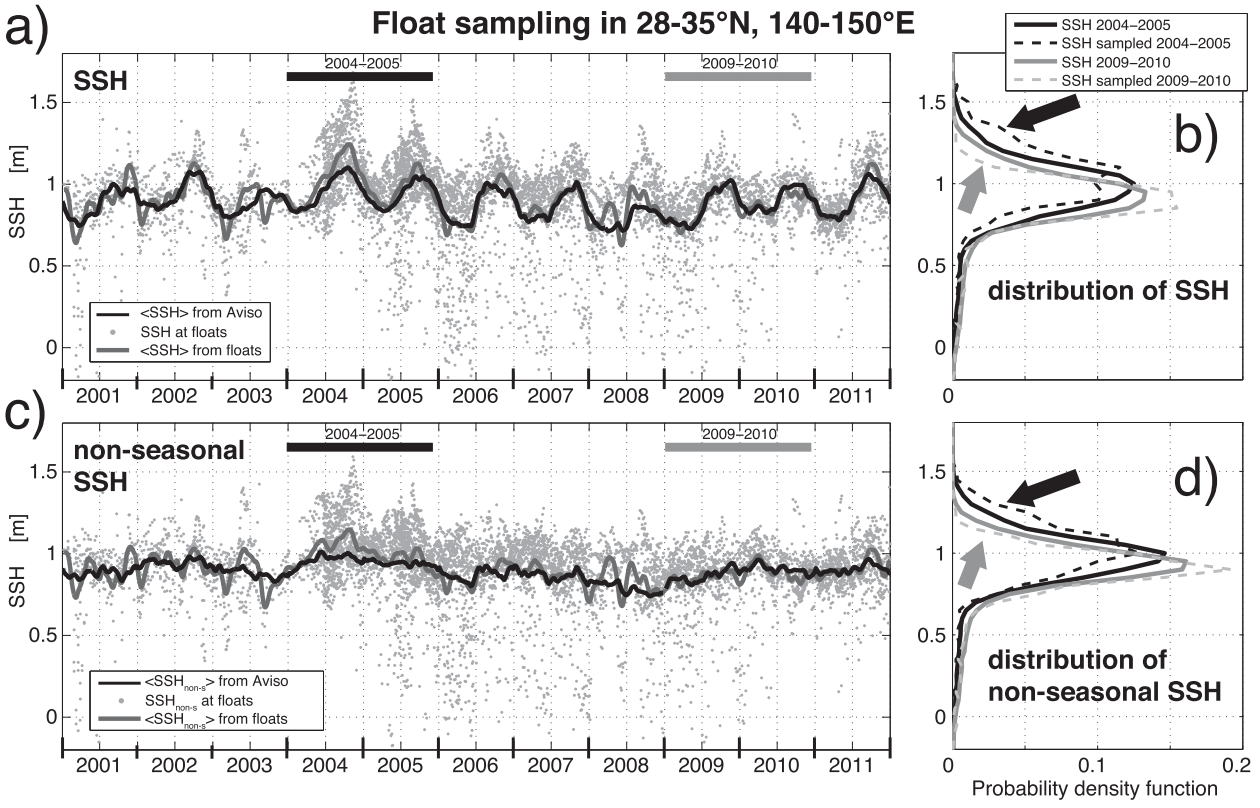

FIG. 5. (a) Time series of the average of the (gridded, from AVISO) SSH in the region 28°–35°N, 140°–150°E from 2002 to 2011 (black line), along with the SSH at every float profile in the same region (gray dots). The average of the SSH sampled by the floats is shown in thick gray. (b) Probability density functions of the SSH in the region (gridded product, solid) and sampled by the floats (dashed) in 2004–05 (black) and 2009–10 (gray). Large arrows point to the biases. (c) Time series of the SSH minus the seasonal average and (d) associated probability density functions.

of each year, followed by the formation of a seasonal thermocline (April–May). Each year, after the formation of the seasonal thermocline, the top of the STMW (and bottom of seasonal thermocline) deepens progressively, eroding into the top of the STMW. In both observational and modeling studies, the distribution of the STMW has been found to be dependent on mesoscale eddies (Uehara et al. 2003; Rainville et al. 2007; Nishikawa et al. 2010) and on the dynamical state of the Kuroshio Extension and of the strength of the recirculation gyre (Qiu and Chen 2006; Qiu et al. 2007a; Douglass et al. 2012). One of the most striking features in the float time series of potential vorticity, highlighted in Qiu et al. (2007a), is the deep pool of STMW in 2004–05 and the subsequent shoaling of the bottom of the STMW. The STMW seems to almost disappear from the recirculation gyre in 2009. The mooring time series, however, shows strong variability in 2006–08 (after the KESS mooring observations), followed by what appears to be a period of thick STMW punctuated by a few eddies. Similarities and differences between these two perspectives are explored below.

Time series of the top and bottom of the STMW, SSH, heat content in the upper 500 m, and mean temperature of the STMW from all float profiles in the region 28°–35°N, 140°–150°E are shown in Fig. 6. For each profile (7085 float profiles in the geographical area, without any restrictions in SSH), the bottom of the STMW layer, the SSH at the time and location of the profile, and the heat content of the upper 500 m are colored by the SSH at the time and location of the profile. The same quantities from the KEO/KESS-7 moorings are shown in black. Note that no SSH conditions are imposed here: by considering floats profiles with a SSH $>$ 0.75 m, Fig. 4 and Qiu et al. (2007a) likely emphasize the contrast between the 2004 weakly meandering period (where floats were seeded in high-SSH regions) and afterward (when floats preferably sampled low-SSH regions).

The estimates of the depths of the top and bottom of STMW from the floats generally agree with that from mooring, but they can also differ significantly (e.g., top of STMW in 2005, bottom 2009). Note that even in the ''weakly meandering'' period (e.g., summer 2004), the

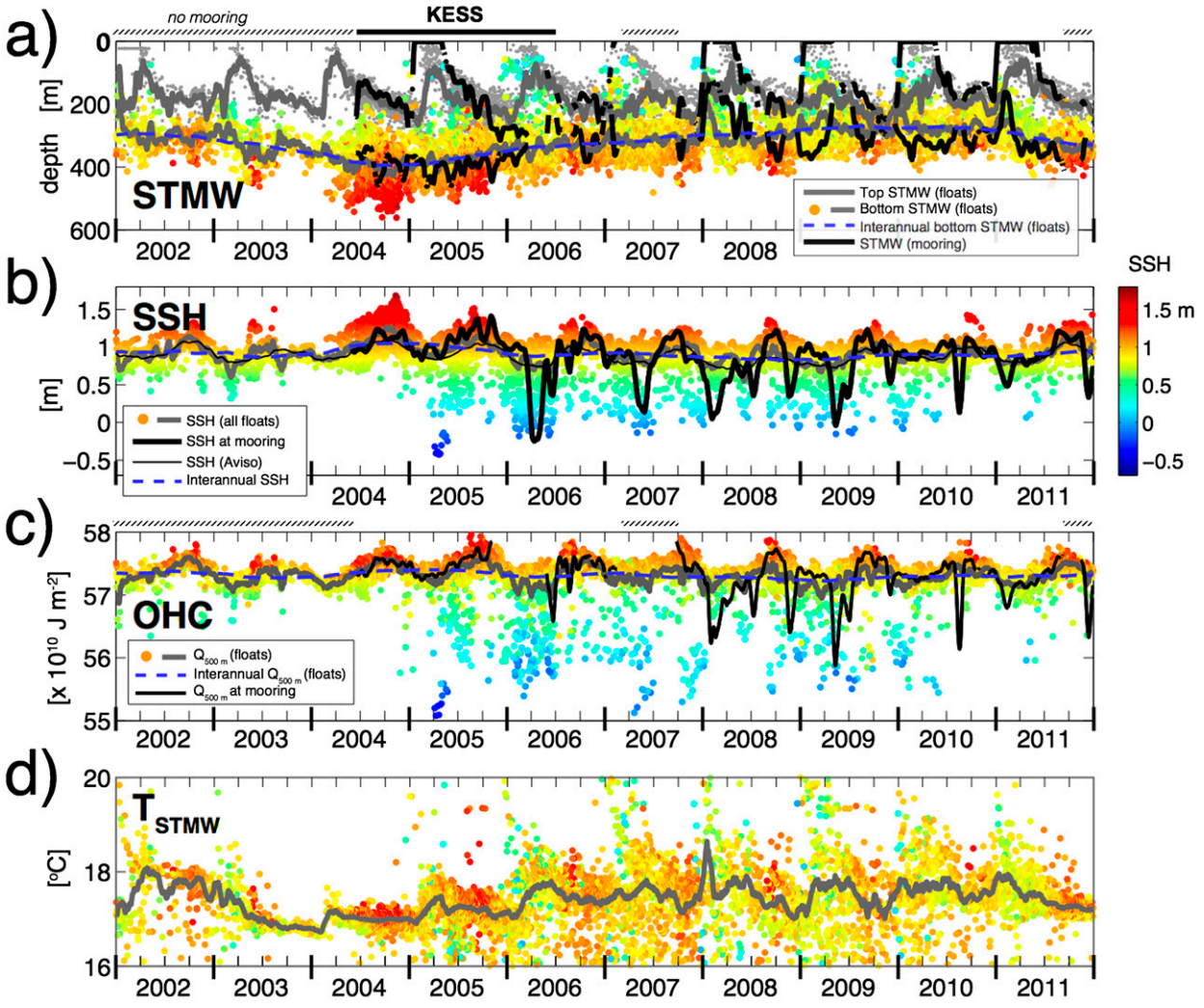

FIG. 6. (a) Top (gray dots) and bottom (dots colored by SSH) of the STMW layer from all the float profiles in the RG. (b) SSH at the location of each profile, (c) OHC for every float profile in the RG, and (d) average temperature of the STMW layer, all colored by SSH. Median from all float profiles smoothed with a 14-day running mean (gray lines), and interannual variations (dashed blue lines) are also shown. For (a)–(c), the corresponding estimates from the KESS/KEO mooring observations are shown in black. In (b), the averaged SSH from the gridded altimetry product in the entire area is shown by the thin black line.

thickness of the STMW can vary by several hundred meters between profiles recorded within the same week. In winter, one can generally find float profiles in the recirculation gyre that capture nonoutcropping STMW, bringing the average top of STMW lower than observed at KEO/KESS 7. There is a general tendency for the deepest estimates of the bottom of STMW to be associated with high values of SSH (associated with strong anticyclonic circulations). The SSH time series at the mooring site highlights several strong cyclonic (low SSH) eddies passing by the mooring starting at the beginning of 2006. Even when averaged over the relatively large recirculation gyre, the interannual variability is significantly less than the variability on shorter time scales, and therefore can easily be biased. Many float profiles (~15%) in the area profiled in locations where SSH was below 0.75 m, the threshold used by Qiu et al. (2007a).

The time series of heat content in the upper 500 m (Fig. 6c) shows a strong seasonal signal. Estimates of heat content from individual float profiles show a relationship with SSH at the profile location. The variability observed in the float matches quite well the magnitude of the variations recorded at the mooring site. These relationships are explored and quantified below.

The temperature of the STMW T_{STMW} does not seem to have much relationship with SSH or the thickness of the STMW, or even heat content. Instead, it can be

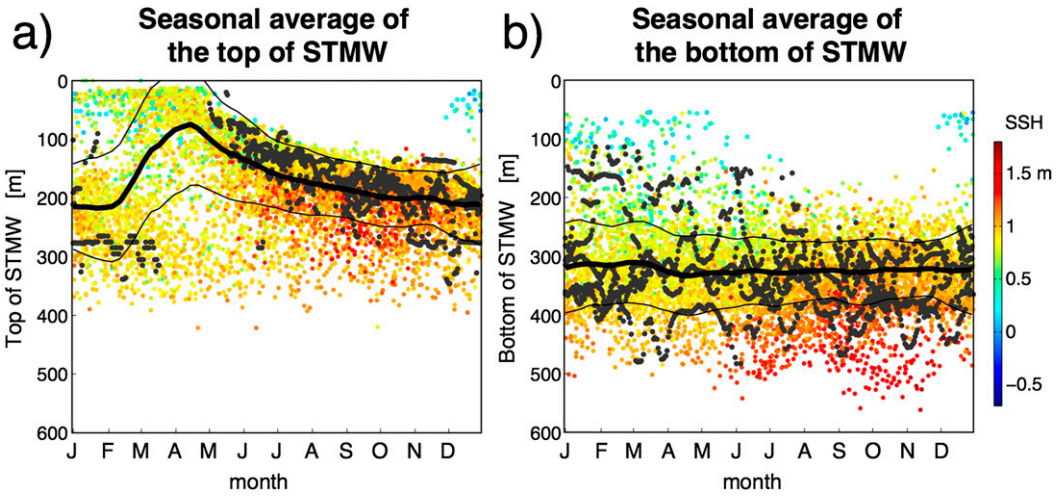

FIG. 7. Depth of the (a) top and (b) bottom of the STMW in the area of the RG (28°–35°N, 140°–150°E) vs calendar month, showing the seasonal average of the STMW. Float data are colored by SSH at the float profile locations, and estimates from the KEO/KESS-7 moorings are shown in black. Median depth is shown by the thick black line, and the median plus or minus one standard deviation is shown by the thin black lines.

primarily characterized by a series of steps, each of which is set by the conditions at the time of the formation of new mode water (March) of the formation. The values likely depend on the preexisting STMW, the magnitude of the air–sea fluxes over a particular outcrop area, etc. We note that, particularly in periods where the Kuroshio jet is most unstable, mode water seems to be formed at many different temperatures (Oka 2009), which mix and evolve over the course of the following year to a narrower distribution of temperatures. More than the ocean heat content (OHC) and the thickness of the STMW, T_{STMW} seems to hold the strongest memory of the formation period. It is included here for completeness, but the lack of relationship with SSH makes it difficult to obtain unbiased maps of the distribution of T_{STMW}. We refer the reader to Oka (2009), for an example on how one can track different ''flavors'' of STMW over several months. Relating the long-term evolution of T_{STMW} relative to SSH and air–sea fluxes during the formation region would be a worthwhile effort for future work.

b. *Top of the STMW: Seasonal and episodic forcing*

The dominant signal in the evolution of the top of the STMW is the seasonal signal (Fig. 7a). The seasonal signal is calculated by binning data into their yearday and doing a 1-month running mean. No obvious correspondence is seen between the depth of the top of the STMW and the SSH (color of the dots). The top of the STMW during March and April is generally shallower (often found at the surface) than during the rest of the year and is generally at its deepest also in late fall/early winter (November–February). In contrast, there is little seasonal variation in the bottom of the STMW (Fig. 7b). In both cases, there is strong variability that is not seasonal, as indicated by the large standard deviations, on average 70 and 60 m for the top and bottom, respectively.

The high-resolution time series recorded at the KEO/KESS-7 moorings during the KESS period provide additional details on the evolution of the mixed layer and STMW: Fig. 8a shows time series of total and latent surface heat flux measured at KEO for the fall 2004 and winter 2005 (Cronin et al. 2013). The time series of potential vorticity, a more detailed view of Fig. 3, is shown in Fig. 8b, together with the wind speed time series (Fig. 8c). Strong atmospheric cooling drives the surface mixed layer to deepen in winter, followed by the establishment of the seasonal thermocline when the atmosphere starts heating the surface. A detailed description of the mixed layer variability can be found in Cronin et al. (2013).

The deepening of the mixed layer is episodic and frequently associated with the passage of typhoons (e.g., Bond et al. 2011). In Fig. 8, the arrows indicate the passage of typhoons Namtheun, Meari, and Tokage, respectively, in the vicinity of KEO (Bond et al. 2010) [see also Fig. 1 of Tomita et al. (2010), for tracks]. Winds over $10\,\mathrm{m\,s^{-1}}$ are observed, and the mixed layer seems to deepen in discrete steps, although the poor vertical resolution of the upper ocean measurements prevents more quantitative estimates.

The MPs crawled up or down the mooring line every 15 h, aliasing the near-inertial frequency to periods of about 2 days (45.4 h at the latitude of KESS 7). The sampling period was chosen to alias the near-inertial and

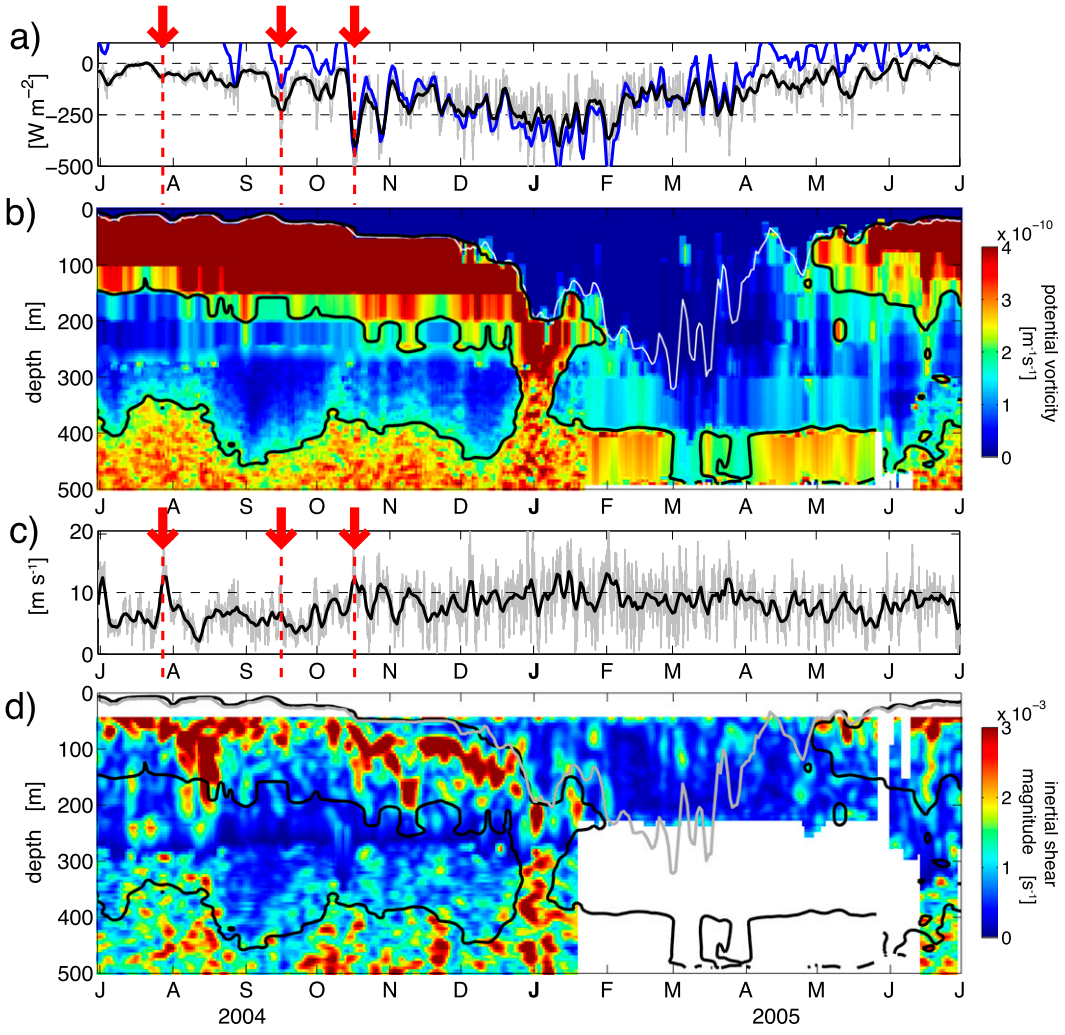

FIG. 8. (a) Time series of the total (blue) and latent (black) surface heat flux, smoothed with a 3-day running mean. Hourly latent heat flux data are shown in gray. (b) Depth–time map of potential vorticity ($Q = 2 \times 10^{-10}\,\mathrm{m^{-1}\,s^{-1}}$ contoured in black), with a time series of the mixed layer depth plotted in white. (c) Hourly (gray) and 3-day smoothed (black) wind speed time series measured at KEO. (d) Depth–time map of the magnitude of inertial shear. $Q = 2 \times 10^{-10}\,\mathrm{m^{-1}\,s^{-1}}$ is contoured in black and mixed layer depth shown in gray. Red arrows in (a) and (c) indicate strong forcing events.

tidal frequencies to a minimum in the spectrum of velocity, between the frequencies where most of the variance of the mesoscale and internal wave bands lie. By bandpassing the MP velocity data around the aliased frequency, the near-inertial velocity and isopycnal displacements in the main thermocline can be inferred with a time scale of about 2.5 days (see appendix). Above 250 m, ADCP data from the subsurface mooring are available with a sampling period of 30 min that can simply be bandpassed (fourth-order Butterworth filter with a bandwidth of $\frac{1}{3}\,\mathrm{day^{-1}}$) to obtain the inertial velocity.

Inertial currents are estimated at each depth and as a function of time, taking only the component that rotates clockwise in time at the local inertial frequency. Figure 8d shows a depth–time map of the magnitude of the velocity shear of the inertial waves. Large wind events, typhoons and strong winter storms, are accompanied by the generation of strong inertial motion in the mixed layer, which propagates vertically through the seasonal thermocline, as shown by the downward propagation of the shear signal in time.

Likewise, the deepening of the seasonal thermocline also appears to be episodic and associated with the passage of typhoons (Tomita et al. 2010), although the relatively coarse vertical resolution of the KEO oceanic sensors makes it less clear. There is a good correspondence between times when strong inertial vertical shear is present at the base of the seasonal thermocline and

TABLE 2. Mean and standard deviations of the interannual, seasonal, and mesoscale variations of the SSH, top, and bottom of STMW; ocean heat content in the upper 500 m; and temperature of the STMW, estimated from all the float profiles in the RG (28°–35°N, 140°–150°E). Percentages of the total variance contained in each band are indicated in parentheses.

	Mean	Interannual	Seasonal	Mesoscale
SSH (m)	0.91	0.06 (7%)	0.08 (10%)	0.21 (77%)
Top of STMW (m)	177	13 (3%)	39 (23%)	74 (84%)
Bottom of STMW (m)	319	40 (30%)	9.0 (2%)	60 (68%)
Heat content (10^{10} J m^{-2})	57.3	0.04 (2%)	0.10 (9%)	0.31 (85%)
T_{STMW} (°C)	17.4	0.20 (11%)	0.11 (4%)	0.55 (84%)

deepening of the top of the STMW, suggesting that enhanced mixing caused by these episodic events is responsible for some of the variability in the STMW thickness. The episodic strong mixing events will cause exchange of fluid between the seasonal thermocline and the STMW layer. Estimates based on the observed inertial shear in the seasonal thermocline indicate that vertical mixing can be significantly enhanced at times, relative to typical values obtained in the midlatitude thermocline. The energetic inertial shear results in large diffusive mixing at the base of the mixed layer, particularly during winter when the stratification is weak (Cronin et al. 2013). Mixing processes, known to be important for the mixed layer budget (Plueddemann and Farrar 2006), are also likely to be important for the erosion of the STMW. It should be noted that mixing, and thus erosion, is highly variable and closely associated with strong wind events (e.g., tropical cyclones traveling over the Kuroshio Extension). This might explain the discrepancies between the estimates of turbulent diapycnal diffusivity from in situ observations obtained over a relatively short period of time (Mori et al. 2008) and the higher values inferred from budget analysis (Qiu et al. 2006; Cronin et al. 2013). A more detailed study of the links between STMW and near-inertial oscillations is needed but is beyond the scope of this paper.

c. *Bottom of the STMW: Mesoscale eddies and basin-scale SSH variability*

The links between the STMW, the dynamical state of the Kuroshio and its eddy activity (as inferred by SSH), and the heat content of the upper 500 m, suggested by the float and mooring data (Fig. 6), are quantified here. In particular, the time series of the depth of the bottom of STMW, SSH, and heat content from the floats are separated into a mean, a low-frequency anomaly (a 1-yr running mean), a seasonal average (obtained from binning data into their yearday and doing a 1-month running mean), and their "mesoscale" component (variations at periods less than seasonal). Ten years of data are used here, and the biases in the distributions (Fig. 5) are ignored. The mean and standard deviations, as well as percentage of variance contained in each band, are listed in Table 2. While the statistics might be slightly biased, the main purpose of this exercise is to obtain relationships that can be used to construct estimates of STMW thickness as a function of gridded SSH (available from satellite) and the seasonal average of the top of the STMW (i.e., time of year), which will be adjusted using in situ data to provide accurate estimates of STMW properties (section 4). The variations of T_{STMW} are included in Table 2 for completeness, even though it shows no correlation to the evolving SSH, STMW thickness, or oceanic heat content fields.

The relationship between the bottom of the STMW and the SSH (Fig. 9a) is mostly evident in the mesoscale variations. Positive anomalies of SSH, corresponding to anticyclonic eddies or a stronger southern recirculation gyre (Qiu and Chen 2005, 2006), are associated with deeper STMW. Conversely, there is little STMW in cyclonic eddies (negative SSH anomalies). Note that the median relationship is close to linear, with a slope of about −270 m of STMW thickness per meter of SSH anomaly. The same types of relationships are present for the seasonal average and interannual trend, mostly for positive SSH anomalies. The differences in the slope for the various periods considered are, at least in part, likely consequences of the biases in the float distribution discussed earlier (Fig. 5). In addition to the direct effect of the mesoscale eddies, these results point toward a link between the low-frequency variability of the STMW and the low-frequency SSH signature of basin-scale phenomena, although these are likely lagged or indirect responses. Indeed, recent studies have suggested that the North Pacific Gyre Oscillation might play an important role in controlling the Kuroshio Extension variability: basinwide wind variability might excite Rossby waves that propagate to the Kuroshio Extension and trigger changes in the intensity of the Kuroshio Extension jet and of its recirculation gyres (Taguchi et al. 2007; Qiu et al. 2007b; Ceballos et al. 2009).

d. *Heat content*

The relationships between the STMW and the total heat content of the upper 500 m of the ocean are displayed in Fig. 9b. There is a general trend that deeper

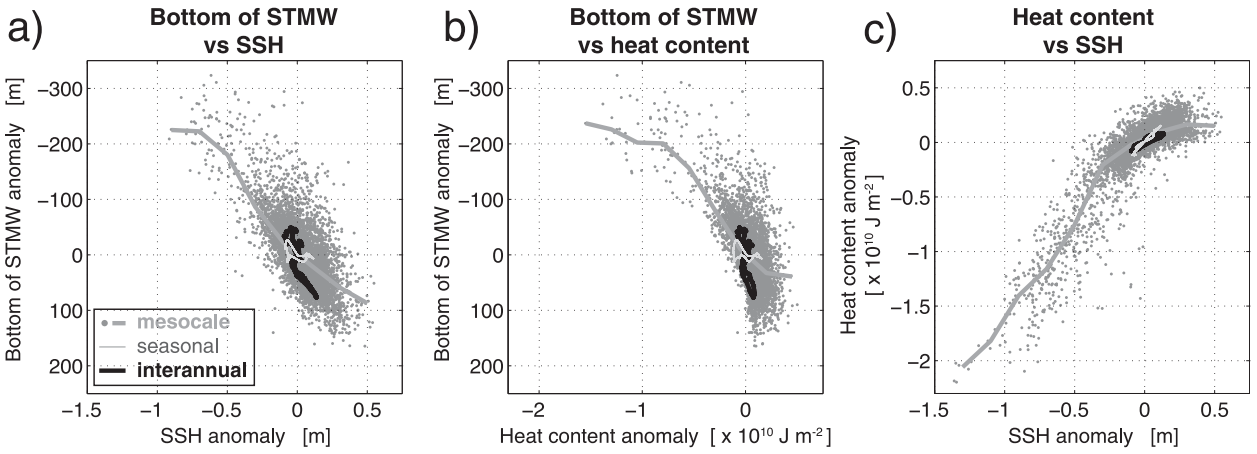

FIG. 9. (a) Depth of the bottom of the STMW anomaly as a function of SSH anomaly for all float profiles in the RG (28°–35°N, 140°–150°E) for the interannual variations (black), seasonal average (light gray), and mesoscale (dark gray). Median relationship for the mesoscale band is shown by the dark gray line. Similar plots are shown for (b) the depth of the bottom of the STMW as a function of heat content anomaly in the upper 500 m and (c) heat content anomaly vs SSH anomaly.

STMW is associated with positive heat content anomalies (deeper STMW corresponds to more heat in the upper 500 m)—an opposite relationship to that found in the North Atlantic, where positive anomalies in STMW (commonly referred as Eighteen Degree Water in the Atlantic) volume are associated to a negative anomaly in heat content (Kelly et al. 2010).

As observed in several earlier studies (e.g., Vivier et al. 2002; Kelly and Dong 2004), the heat content anomalies are strongly related to the SSH anomalies (Fig. 9c). The quasi-linear relationship, where a 0.5-m rise in SSH corresponds to an increase of almost $1 \times 10^{10}\,\mathrm{J\,m^{-2}}$ in heat content of the upper 500 m, somewhat breaks down for SSH anomalies larger than 0 m. This is likely a consequence of the depth to which we chose to integrate the heat content: positive SSH anomalies also correspond to times when the bottom of the STMW layer approaches 500 m (when depressing the thermocline further has little impact on the properties above 500 m).

Ultimately, the interannual variations of SSH and heat content are small and generally consistent with each other, while the STMW appears to vary more widely on interannual time scales than predicted using the relationship between SSH and STMW (or heat content and STMW) for shorter time scales. In all cases, the interannual signal is buried in the very complex mesoscale variability and is very sensitive to small biases in the float sampling distribution. These small biases resulting from the distribution of the observations, for example, or attributable to the dominance of eddies at single point measurements, are likely to obscure the links on time scales of months to years. For this reason, the relationships among ocean heat content, SSH, and STMW are revisited in section 5 using the nonbiased estimates derived below.

4. Maps of STMW and heat content

The dominant relationship between the SSH and the STMW can be used to produce a first estimate of the spatial and temporal distribution of the STMW. Over the entire western North Pacific, the seasonal dependence of the top of the STMW is estimated as the median of the estimates from all the float profiles (as in Fig. 7a) separately for a series of overlapping regions of 2.5° of latitude by 5° of longitude. The side of the boxes was chosen as a compromise between obtaining reasonable statistics (as in Fig. 9a) while allowing spatial variations. Similarly, the (generally) small seasonal signal at the bottom of the STMW is estimated. Most importantly, the relationship between the bottom of the STMW and the nonseasonal SSH is estimated as a function of location. For simplicity, it is assumed that the bottom of the STMW is a linear function of SSH, a reasonable assumption in the example presented in Fig. 9 (over a larger region), except for very large negative SSH (strong cyclonic eddies and very shallow STMW).

Using the climatological relationship between SSH and STMW as a function of location across the entire western North Pacific, the thickness of the STMW can be estimated using gridded maps of SSH: the top of the STMW mainly depends on location and time of the year (seasonal average), and the bottom of the STMW is primarily a function of the SSH variations associated with eddies and interannual variations in the strength of

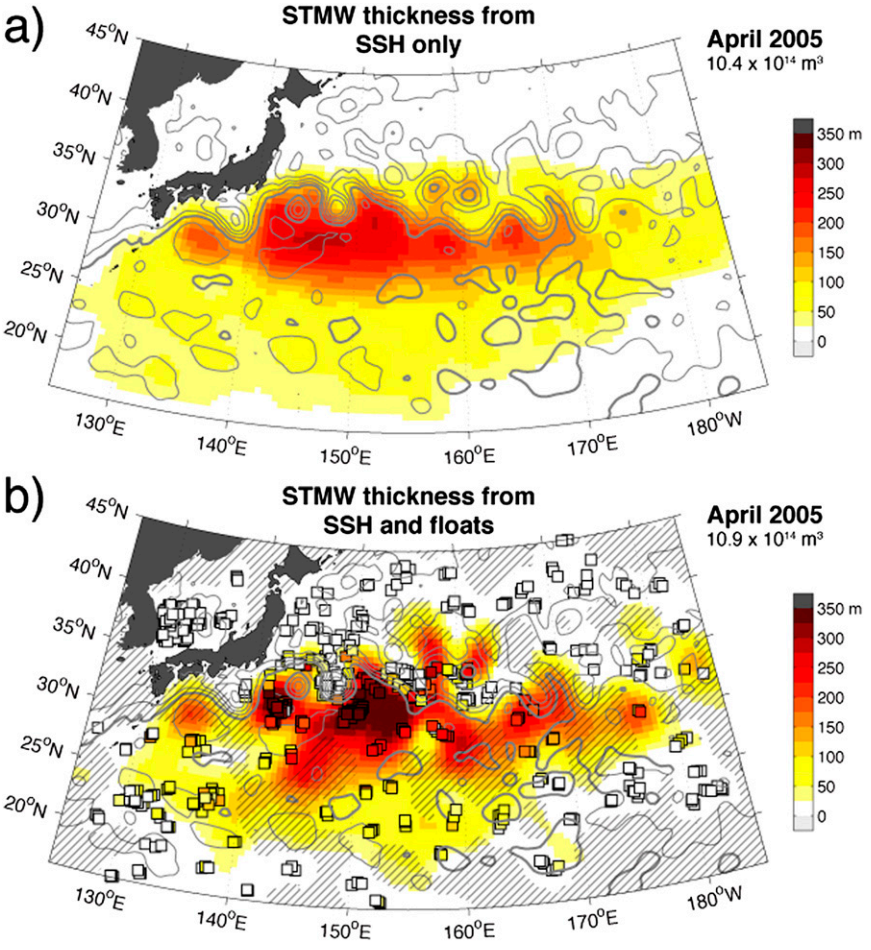

FIG. 10. Maps of the thickness of STMW in mid-April 2005, (a) based on SSH only and (b) from the floats using the SSH map as a starting point. Individual estimates from floats are shown by the color-filled squares, and regions ill constrained by the floats are displayed as the gray hatching. Total STMW volume is listed on the top-right corner in (a) and (b).

the recirculation gyre. Thickness is taken as the difference between the top and bottom, limited to be zero or greater. For example, the estimated thickness of the STMW for the week of 15 April 2005 from the corresponding SSH map is shown in Fig. 10a.

The float array allows us to further constrain these first estimates. Particularly on interannual time scales, float data (Fig. 9a) show that some of STMW variations are not associated with an SSH signal. Using the SSH-based maps as a starting point (as the ''mean''), individual STMW thickness estimates from float profiles collected around the time of the map are used to construct a nonbiased objective map of the STMW thickness, using a decorrelation scale of 300 km. A triangular window with a half-width of 2 weeks is used in time, decreasing the weight given to a float profile collected much before or after from the time of the estimate. These time and spatial scales are similar to those used to generate the AVISO gridded SSH maps (Ducet et al. 2000). In other words, the SSH-based map is adjusted to better reflect the measurements taken during a particular period. Under these prior assumptions, the objective mapping also provides an estimate of where the map is accurate and a quantitative measure of how the addition of float data improved the map in regions where data are available. The STMW thickness map for April 2005 from floats is shown in Fig. 10b. Poorly constrained areas are shown by the hatched regions.

The monthly maps of STMW thickness are obtained every week and can be integrated to estimate the total volume of STMW. The time series of the total STMW volume (over the entire western North Pacific) is shown in Fig. 11a. The volume contained in the ill-constrained areas can be used as a measure of the uncertainty associated with the total volume. The error in the total estimates is estimated by scaling the integrated unconstrained volume

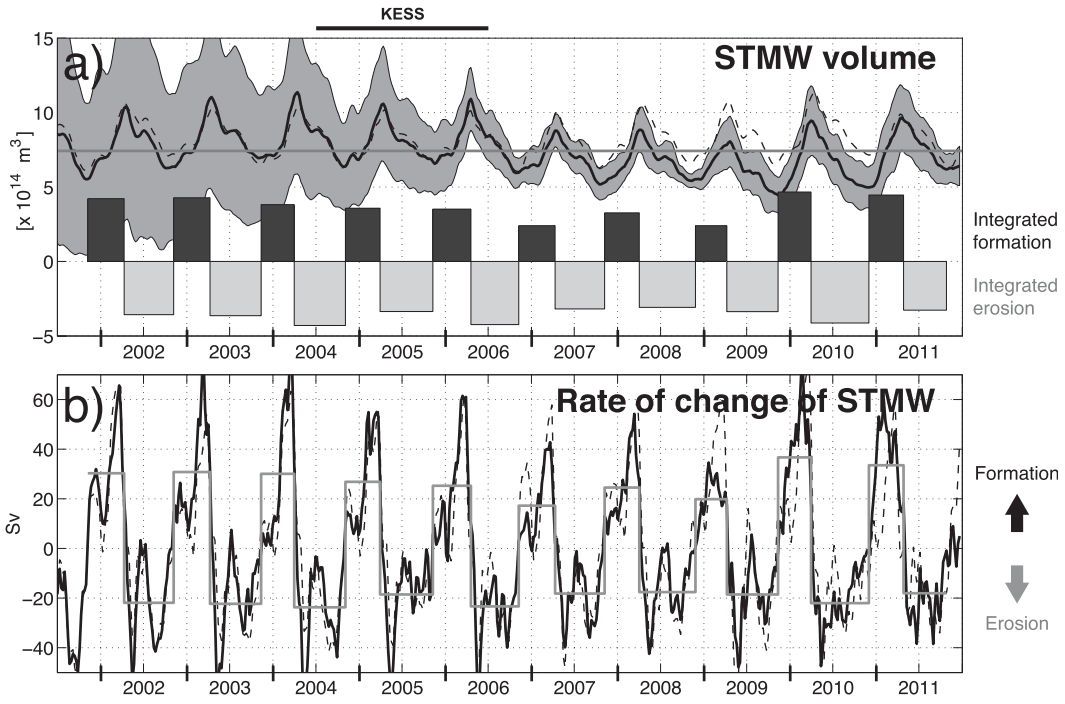

FIG. 11. (a) Total volume of STMW in the western North Pacific as a function of time, obtained from the SSH-based maps adjusted by the Argo float array (thick black line) and by the SSH-based maps only (dashed). The range of volume of STMW accounted for by the unconstrained portion of the floats maps is shown as the gray shading. Integrated formation (positive rate of change, generally February–April) and erosion (negative rate of change) volumes for each year are shown as the black and graybars, respectively. (b) Rate of change of the STMW volume from the floats maps (black, SSH-based maps adjusted by the Argo float array) and SSH-based maps only (dashed). Mean rates over the formation/erosion period are shown in gray.

by the relative error between the SSH-only and constrained maps over areas where floats profiles are present. Over the last 10 yr, the total volume of STMW is, on average, $7.4 \pm 0.2 \times 10^{14}\,m^3$ and does not show clear long-term trends. Large interannual variations are observed: for example, relative to 2004–05 and to 2011, a smaller volume of STMW was present between 2007 and 2010. The volume estimate solely based on the SSH maps is shown as the dashed line. While the time series are very similar, the estimate based only on SSH misses the STMW thinning observed between 2007 and 2010. The SSH-only maps overpredict the formation, presumably because formation of STMW strongly depends on where eddies are located during the short period of strong winter forcing.

The rate of change of STMW volume (Fig. 11b) shows formation happening in winter [positive rate change, up to 70 Sv ($1\,Sv \equiv 10^6\,m^3\,s^{-1}$)], followed by erosion (negative rate of changes) for the rest of the year. Integrated formation volume (over the times when the rate of change is positive) and integrated erosion volume (the rest of the year) for each year are shown by the bars in Fig. 11a and listed, along with the total volume for each year, in Table 3. The average volume of STMW formed each year in the North Pacific is $3.7 \times 10^{14}\,m^3$, and $3.6 \times 10^{14}\,m^3$ are eroded every year, corresponding to rates of 27.5 Sv and −20.4 Sv, respectively.

The interannual variations of STMW volume seem to be mostly associated with variations in the volume of STMW formed each year. The amount of STMW eroded each year is roughly the same, but only about half of the average amount of STMW was formed in 2007 and 2009, resulting in a decrease of volume. During those years, there is no significant change in the average SSH or in the standard deviation of the SSH in the formation region relative to 2006 or 2008. After 2005, the maps are well constrained by the floats. As was found in numerical models (e.g., Rainville et al. 2007), we argue that this suggests that the exact timing of winter storms versus the position of eddies and of the Kuroshio is critical in establishing how much mode water can be formed.

The mapping described here is also used to generate nonbiased maps of the oceanic heat content (OHC) in the upper 500 m for the entire western North Pacific: the relationship between the gridded SSH evaluated at the float profile location and the heat content estimates from

TABLE 3. Volume of STMW for each year (10^{14} m^3; from 1 November of the previous year to 30 October) from the float constrained maps. Uncertainties are all close to 0.2×10^{14} m^3.

Year	2002	2003	2004	2005	2006	2007	2008	2009	2010	2011	Average
Total volume	7.7	8.3	8.3	8.0	8.0	6.9	6.8	6.2	6.6	7.3	7.4 ± 0.2
Formation volume	4.2	4.3	3.8	3.6	3.5	2.4	3.3	2.4	4.7	4.5	3.7 ± 0.2
Erosion volume	−3.6	−3.6	−4.3	−3.4	−4.2	−3.2	−3.1	−3.4	−4.1	−3.3	−3.6 ± 0.2

each profile is calculated as a function of location (in overlapping regions of 2.5° of latitude by 5° of longitude), and the resulting estimates of oceanic heat content from the time varying SSH maps from AVISO are adjusted using the float estimate, with space and time scales comparable to those used in the objective mapping of SSH. The maps (Fig. 12) give a nonbiased estimate of the upper ocean heat content in the top 500 m.

5. Relationship among STMW, ocean heat content, and air–sea heat fluxes

A comprehensive analysis of how STMW influences air–sea fluxes is beyond the scope of this paper. However, here we briefly show how relationships among mode waters, oceanic heat content, and surface heat fluxes can be investigated using nonbiased estimates derived above. The air–sea latent and sensible heat fluxes are obtained from objectively analyzed air–sea fluxes (OAFlux) analysis, a consistent, multidecade, global analysis of air–sea heat fluxes (Yu et al. 2004), averaged over the RG region (28°–35°N, 140°–150°E).

The seasonal averages (Fig. 13a) show the sharp increase of STMW thickness associated with the end of the strong winter cooling of the ocean by the atmosphere. As before, the seasonal averages are obtained from binning data into their yearday and doing a 1-month running mean. As the anomalous heat fluxes become negative in mid-March, the seasonal thermocline begins to form, increasing the upper OHC. On interannual and multimonth time scales (Figs. 13b,c), the relationships are not as obvious. For these longer time scales, the seasonal cycles

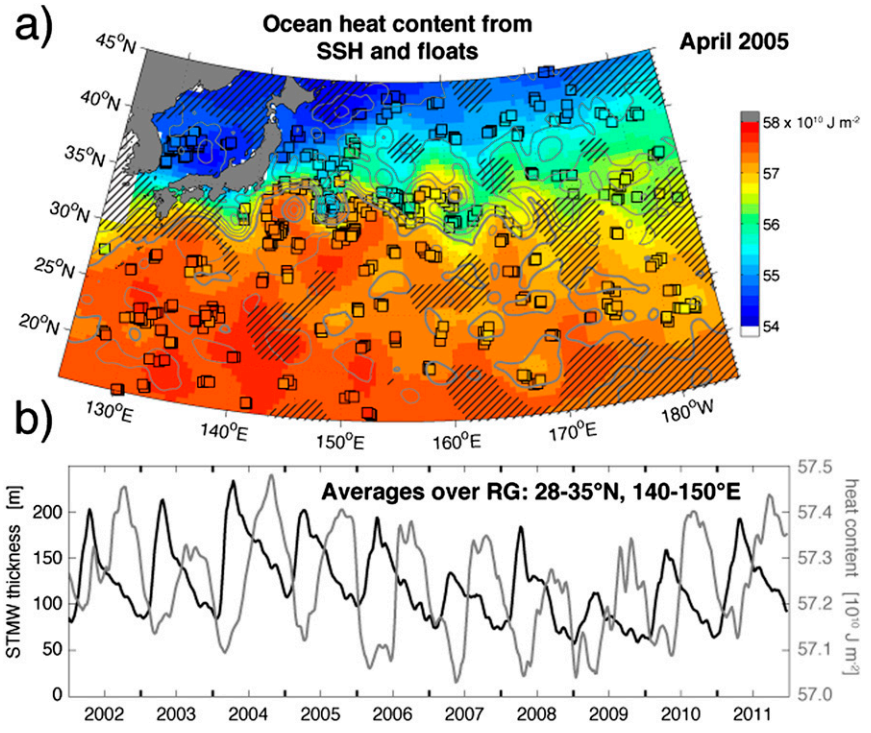

FIG. 12. (a) Map of the OHC in the upper 500 m in mid-April 2005 based the floats using the SSH-derived map as a starting point. Individual estimates from floats are shown by the color-filled squares, and regions ill constrained by the floats are displayed as the gray hatching. (b) Time series of average STMW thickness and heat content in the RG.

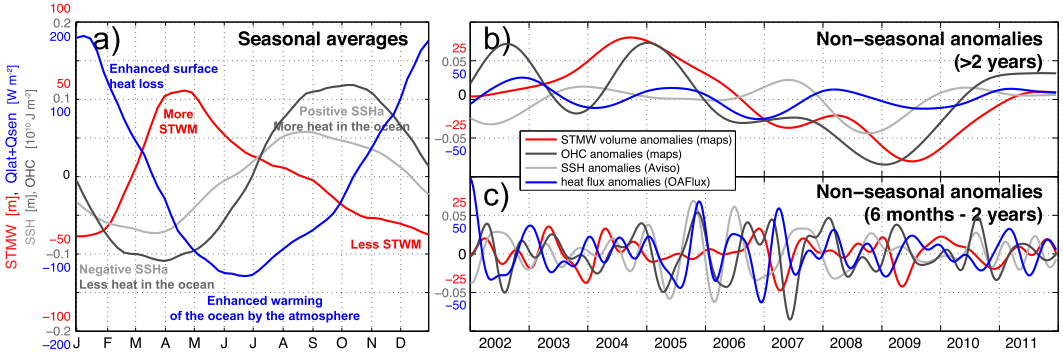

FIG. 13. Nonbiased (a) seasonal and (b),(c) nonseasonal variability of the STMW thickness (dashed), OHC (dark gray), SSH (light gray), and surface heat fluxes (blue), averaged over the RG region (28°–35°N, 140°–150°E). The scale is the same for each panel: thickness of the STMW (m, red), surface heat flux (W m^{-2}, blue), and SSH (m) and OHC (10^{10} J m^{-2}) share the same labels, in gray.

(Fig. 13a) are first removed from the time series and are then low passed (Fig. 13b) or bandpassed (Fig. 13c). In both cases, there are instances when a positive anomaly in heat content or SSH leads to enhanced cooling of the ocean (positive heat flux anomaly) a few months later, as described in Kelly et al. (2010). Signatures of negative correlations, where positive heat flux anomalies lead negative SSH anomalies 4–5 months later—a possible signature of basinwide decadal variability suggested by Taguchi et al. (2007), Qiu et al. (2007b), and Ceballos et al. (2009)—might be also present. None of these correlations are statistically significant, reproducing the results previously observed by Kelly et al. (2010). It may be that a relation exists but is being obscured by other regional or temporal variations. Further work using these nonbiased estimates, potential over larger areas or longer time series, is needed to investigate these relationships. Finally, we note that while heat content and SSH are generally well correlated, many of their fluctuations differ or show a lagged relationship. In particular, the ocean tends to retain heat later in the fall than the SSH time series alone would suggest.

6. Summary and discussion

Direct observations of the STMW from mooring and floats reveal strong variability that can only be explained in part by the dynamical state of the Kuroshio and the presence of eddies. Across the entire western North Pacific, the depth of bottom of the STMW is tightly related to the SSH signature of mesoscale eddies. The top of the STMW and the mixed layer depth seem to be mostly affected by episodic events and vary in discrete steps. The cooling associated with cold air outbreaks plays an important role in the erosion of the seasonal thermocline. The mechanical mixing resulting from the generation of inertial motions by the wind stress propagating as internal waves is also found to be large and very episodic.

There are only a few previous estimates of the total volume of North Pacific STMW from observations—most previous observational studies focus on describing the properties of the core STMW in the Kuroshio Extension region (e.g., Qiu and Chen 2006; Oka 2009; Oka et al. 2011). The technique described here takes into account interannual variations in SSH as well as rapid (and large) changes attributable to both seasonal forcing and the complex impact of the strong mesoscale eddy field. The total STMW volume from the maps (Fig. 11a) is similar to that estimated in high-resolution models. For example, Ladd and Thompson (2001) estimate the total volume of STMW in an isopycnal model varies between 3.2 and 9.7×10^{14} m^3, and Davis et al. (2011) estimate that the net volume of STMW in a (unconstrained) global ocean simulation model varies between about 3.7 and 8.2×10^{14} m^3, with very similar total formation and erosion volumes (both 4.5×10^{14} m^3) to what is found in the observations (Table 3).

We note that the time series of STMW volume (Fig. 11a) summed over the entire western North Pacific appears to be less variable than the decadal variability in the thickness of the STMW in the recirculation gyre (Qiu and Chen 2006; Figs. 4c and 6a) or, similarly, than the time series of potential vorticity in the Kuroshio Extension region from an ocean reanalysis (Miyazawa et al. 2009). Part of the difference can be explained by potential biases in the distribution of the floats (Fig. 5), but this is probably mostly a signature of the redistribution of the STMW on a regional scale by mesoscale eddies and by the contraction and expansion of the recirculation gyre on a multiyear time scale. Changes in the total volume of STMW seem to be primarily linked

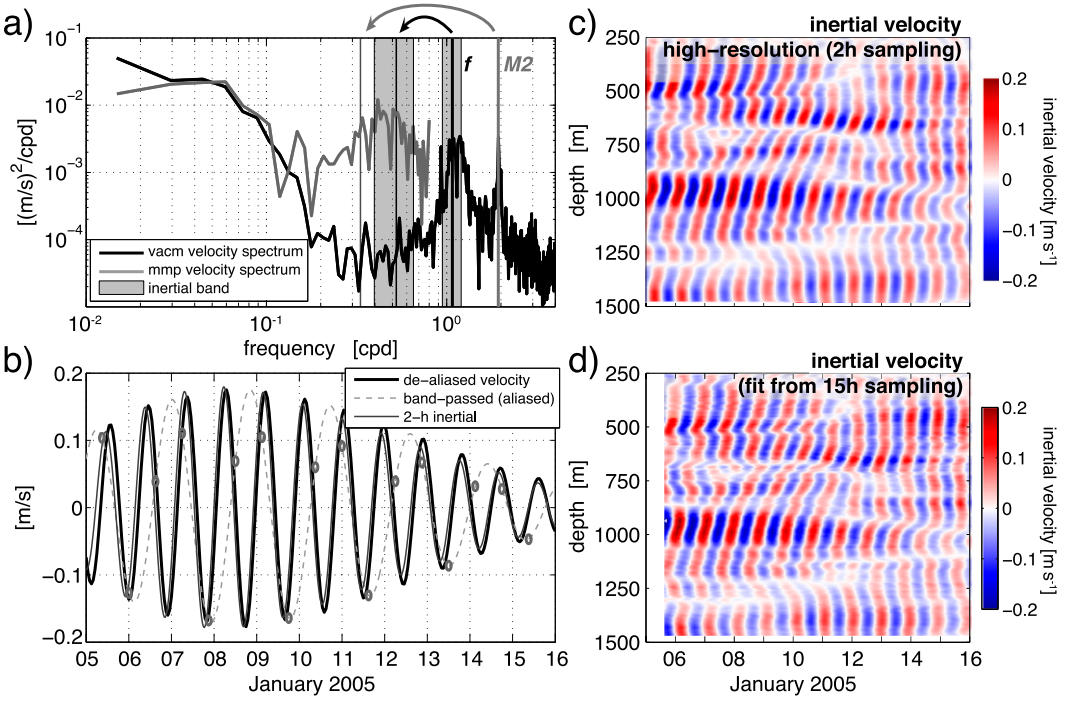

FIG. A1. (a) Frequency spectrum of eastward velocity near 1500 m from a current meter sampling every 30 min (black) and from the MP sampling every 15 h (gray). The inertial (shaded band, $f = 1.07$ cpd) and semidiurnal ($M_2 = 1.93$ cpd) frequencies are aliased in the MP records. Bandwidth of the filter used in the de-aliasing procedure is shown in gray. (b) MP data (gray circle) near 1000 m, bandpassed estimate around the aliased frequency (gray dashed line), and estimate of inertial frequency signal (black line). This example is taken during a time when the MP sampled every 2 h, and the true inertial signal (bandpassed with the same bandwidth) is shown by the thin gray line. (c) Inertial velocity from MP sampling every 2 h and bandpassed around the true inertial frequency, and (d) subsampled every 15 h and de-aliased.

to the formation volume, which in turn is highly dependent on the atmospheric and oceanic conditions over the Kuroshio Extension during a relatively short period in late winter.

The observational formation and erosion volume estimates presented here and high-resolution numerical simulations (Davis et al. 2011) show that variability at small time and spatial scales, particularly during the winter ventilation period, is important for setting the properties of STMW and its impact on climate. The complex relationships among STWM, heat content, and surface heat fluxes need to be further explored in both models and observations.

Finally, we emphasize the importance of monitoring the STMW, both with a large Argo network and moorings, such as the KEO and the recently deployed Japan Agency for Marine-Earth Science and Technology (JAMSTEC) S1 site (near 30°N, 145°E) to provide direct observations to calibrate and validate models (Cronin et al. 2010). Our analysis also indicates the need for direct velocity measurements, as internal waves appear to play an important role in the evolution of the seasonal thermocline and formation of STMW.

Acknowledgments. We gratefully acknowledge the WHOI Subsurface Mooring Group and thank the captains and crews of the R/V *Thompson*, R/V *Roger Revelle*, and R/V *Melville* for their support of the KESS mooring operations. This work was sponsored by the National Science Foundation (Grants OCE-0220161, OCE-0825152, and OCE-0827125). More details about KESS can be found at http://uskess.org/. The KEO time series reference site is sponsored by the National Oceanic and Atmospheric Administration (NOAA) Office of Climate Observations (OCO). KEO mooring data are available from the PMEL Ocean Climate Stations web pages at http://www.pmel.noaa.gov/ocs/KEO. All STMW and OHC maps and derived products are available from the KESS web page (http://uskess.org). Argo data were collected and made freely available by the International Argo program and the national programs that contribute to it (http://www.argo.ucsd.edu; http://argo.jcommops.org). The Argo program is part of the Global Ocean Observing System. The ocean heat flux products were provided by the WHOI OAFlux project funded by the NOAA Climate Observations and Monitoring program. The altimeter products were produced by Ssalto/Duacs

and distributed by AVISO, with support from CNES (http://www.aviso.oceanobs.com/duacs/).

APPENDIX

Inertial Signal from Moored Profilers

To collect 1250-m long profiles for an entire year, the MPs deployed during KESS had to be programmed to profile only once every 15 h. The semidiurnal and inertial frequency signals are therefore aliased in the MP records. For example, Fig. A1a shows the frequency spectrum of east velocity from a vector-average current meter (VACM) located at 1500 m, just below the profiling range of the MP, and the spectrum of velocity from the MP, just above the VACM (~20 m above). The variance located at inertial frequency f and lunar semidiurnal frequency M_2 is aliased in the MP record to frequencies corresponding to periods of 45.7 and 72.2 h, respectively (arrows in Fig. A1a). The sampling period of the MPs was chosen because the aliased frequencies of these dominant motions fall in a frequency range where the oceanic variance is minimum, between mesoscale range and the internal wave band (i.e., between 10^{-1} cycles per day and f).

The equivalent of a complex demodulation needs to be performed to retrieve the inertial frequency. The time series data from the MP (gray circles in Fig. A1b) are bandpassed around the aliased frequency using a fourth-order Butterworth filter with a bandwidth equal to $0.25\,\text{day}^{-1}$. For illustrative purposes, the 7-day running average of velocity was subtracted to the MP data before plotting. The amplitude and phase of the resulting signal (gray line in 14b) can be used with the original frequency to obtain the de-aliased inertial estimate (black line).

In early January 2005, a software glitch made the MP of the subsurface mooring nearest to KEO (KESS 7) profile every 2 h (also 250–1500 m), thus resolving the near-inertial frequencies for almost a month during strong winter forcing, before running out of power later that month. This period, although unfortunate since it exhausted the MP batteries several months before the end of the deployment, allows us to validate this procedure. Inertial signals can be directly calculated using a band-pass Butterworth filter with the same bandwidth as the one used in the aliased procedure (Figs. A1c,d). The MP data in January 2005 are subsampled every 15 h and the de-aliasing procedure is carried out. The two estimates are similar. The velocity variance of the two fields is exactly the same ($2.7 \times 10^{-3}\,\text{m}^2\,\text{s}^{-2}$), which is 3 times larger than the variance of the difference. With this technique, the inertial wave field was estimated at several mooring sites during KESS from near the surface (using the ADCPs) to nearly 1500 m.

REFERENCES

Alexander, M. A., and C. Deser, 1995: A mechanism for the recurrence of midlatitude SST anomalies during winter. *J. Phys. Oceanogr.,* **25,** 122–137, doi:10.1175/1520-0485(1995)025<0122:AMFTRO>2.0.CO;2.

Bingham, F. M., 1992: Formation and spreading of subtropical mode water in the North Pacific. *J. Geophys. Res.,* **97,** 11 177–11 189, doi:10.1029/92JC01001.

Bond, N. A., and M. F. Cronin, 2008: Regional weather patterns during anomalous air–sea fluxes at the Kuroshio Extension Observatory (KEO). *J. Climate,* **21,** 1680–1697, doi:10.1175/2007JCLI1797.1.

——, ——, and M. Garvert, 2010: Atmospheric sensitivity to SST near the Kuroshio Extension during the extratropical transition of Typhoon Tokage. *Mon. Wea. Rev.,* **138,** 2644–2663, doi:10.1175/2010MWR3198.1.

——, ——, C. Sabine, Y. Kawai, H. Ichikawa, P. Freitag, and K. Ronnholm, 2011: Upper ocean response to Typhoon Choi-Wan as measured by the Kuroshio Extension Observatory mooring. *J. Geophys. Res.,* **116,** C02031, doi:10.1029/2010JC006548.

Ceballos, L., E. D. Lorenzo, C. D. Hoyos, N. Schneider, and B. Taguchi, 2009: North Pacific Gyre Oscillation synchronizes climate fluctuations in the eastern and western North Pacific. *J. Climate,* **22,** 5163–5174, doi:10.1175/2009JCLI2848.1.

Cronin, M. F., C. Meinig, C. L. Sabine, H. Ichikawa, and H. Tomita, 2008: Surface mooring network in the Kuroshio Extension. *IEEE Syst. J.,* **2,** 424–430, doi:10.1109/JSYST.2008.925982.

——, and Coauthors, 2010: Monitoring ocean–atmosphere interactions in western boundary current extensions. *Proceedings of OceanObs'09: Sustained Ocean Observations and Information for Society,* J. Hall, D. E. Harrison, and D. Stammer, Eds., Vol. 2, ESA Publ. WPP-306, ESA, 11 pp., doi:10.5270/OceanObs09.cwp.20.

——, and Coauthors, 2013: Formation and erosion of the seasonal thermocline in the Kuroshio Extension Recirculation Gyre. *Deep-Sea Res. II,* **85,** 62–74, doi:10.1016/j.dsr2.2012.07.018.

Davis, X. J., L. M. Rothstein, W. K. Dewar, and D. Menemenlis, 2011: Numerical investigations of seasonal and interannual variability of North Pacific Subtropical Mode Water and its implications for Pacific climate variability. *J. Climate,* **24,** 2648–2665, doi:10.1175/2010JCLI3435.1.

Donohue, K., and Coauthors, 2008: Program studies in the Kuroshio Extension. *Eos, Trans. Amer. Geophys. Union,* **89,** 161–162, doi:10.1029/2008EO170002.

Douglass, E. M., S. R. Jayne, S. Peacock, F. O. Bryan, and M. E. Maltrud, 2012: Subtropical mode water variability in a climatologically forced model in the northwestern Pacific Ocean. *J. Phys. Oceanogr.,* **42,** 126–140, doi:10.1175/2011JPO4513.1.

Ducet, N., P. Y. Le Traon, and G. Reverdin, 2000: Global high-resolution mapping of ocean circulation from TOPEX/Poseidon and ERS-1 and -2. *J. Geophys. Res.,* **105,** 19 477–19 498, doi:10.1029/2000JC900063.

Hanawa, K., and L. D. Talley, 2001: Mode waters. *Ocean Circulation and Climate,* G. Siedler, J. Church, and J. Gould, Eds., International Geophysics Series, Vol. 77, Academic Press, 373–386.

Jayne, S. R., and Coauthors, 2009: The Kuroshio Extension and its recirculation gyres. *Deep-Sea Res. I,* **56,** 2088–2099, doi:10.1016/j.dsr.2009.08.006.

Kelly, K. A., and S. Dong, 2004: The relationship of western boundary current heat transport and storage to mid-latitude ocean-atmosphere interaction. *Earth's Climate: The*

Ocean-Atmosphere Interaction, Geophys. Monogr., Vol. 147, Amer. Geophys. Union, 347–363, doi:10.1029/147GM19.

——, R. J. Small, R. M. Samelson, B. Qiu, T. M. Joyce, Y. O. Kwon, and M. F. Cronin, 2010: Western boundary currents and frontal air–sea interaction: Gulf Stream and Kuroshio Extension. *J. Climate,* **23,** 5644–5667, doi:10.1175/2010JCLI3346.1.

Konda, M., H. Ichikawa, H. Tomita, and M. F. Cronin, 2010: Surface heat flux variations across the Kuroshio Extension as observed by surface flux buoys. *J. Climate,* **23,** 5206–5221, doi:10.1175/2010JCLI3391.1.

Ladd, C., and L. A. Thompson, 2001: Water mass formation in an isopycnal model of the North Pacific. *J. Phys. Oceanogr.,* **31,** 1517–1537, doi:10.1175/1520-0485(2001)031<1517:WMFIAI>2.0.CO;2.

Legg, S., and J. C. McWilliams, 2002: Sampling characteristics from isobaric floats in a convective eddy field. *J. Phys. Oceanogr.,* **32,** 527–534, doi:10.1175/1520-0485(2002)032<0527:SCFIFI>2.0.CO;2.

Masuzawa, J., 1969: Subtropical mode water. *Deep-Sea Res. Oceanogr. Abstr.,* **16,** 463–472, doi:10.1016/0011-7471(69)90034-5.

Maximenko, N., P. Niiler, M.-H. Rio, O. Melnichenko, L. Centurioni, D. Chambers, V. Zlotnicki, and B. Galperin, 2009: Mean dynamic topography of the ocean derived from satellite and drifting buoy data using three different techniques. *J. Atmos. Oceanic Technol.,* **26,** 1910–1919, doi:10.1175/2009JTECHO672.1.

Miyazawa, Y., and Coauthors, 2009: Water mass variability in the western North Pacific detected in a 15-year eddy resolving ocean reanalysis. *J. Oceanogr.,* **65,** 737–756, doi:10.1007/s10872-009-0063-3.

Mori, K., K. Uehara, T. Kameda, and S. Kakehi, 2008: Direct measurements of dissipation rate of turbulent kinetic energy of North Pacific Subtropical Mode Water. *Geophys. Res. Lett.,* **35,** L05601, doi:10.1029/2007GL032867.

Nishikawa, S., H. Tsujino, K. Sakamoto, and H. Nakano, 2010: Effects of mesoscale eddies on subduction and distribution of subtropical mode water in an eddy-resolving OGCM of the western North Pacific. *J. Phys. Oceanogr.,* **40,** 1748–1765, doi:10.1175/2010JPO4261.1.

Oka, E., 2009: Seasonal and interannual variation of North Pacific Subtropical Mode Water in 2003–2006. *J. Oceanogr.,* **65,** 151–164, doi:10.1007/s10872-009-0015-y.

——, and B. Qiu, 2012: Progress of North Pacific mode water research in the past decade. *J. Oceanogr.,* **68,** 5–20, doi:10.1007/s10872-011-0032-5.

——, T. Suga, C. Sukigara, K. Toyama, K. Shimada, and J. Yoshida, 2011: ''Eddy resolving'' observation of the North Pacific Subtropical Mode Water. *J. Phys. Oceanogr.,* **41,** 666–681, doi:10.1175/2011JPO4501.1.

Plueddemann, A. J., and J. T. Farrar, 2006: Observations and models of the energy flux from the wind to mixed-layer inertial currents. *Deep-Sea Res. II,* **53,** 5–30, doi:10.1016/j.dsr2.2005.10.017.

Qiu, B., and S. Chen, 2005: Variability of the Kuroshio Extension jet, recirculation gyre and mesoscale eddies on decadal timescales. *J. Phys. Oceanogr.,* **35,** 2090–2103, doi:10.1175/JPO2807.1.

——, and ——, 2006: Decadal variability in the formation of the North Pacific Subtropical Mode Water: Oceanic versus atmospheric control. *J. Phys. Oceanogr.,* **36,** 1365–1380, doi:10.1175/JPO2918.1.

——, P. Hacker, S. Chen, K. A. Donohue, D. R. Watts, H. Mitsudera, N. G. Hogg, and S. R. Jayne, 2006: Observations of the subtropical mode water evolution from the Kuroshio Extension System Study (KESS). *J. Phys. Oceanogr.,* **36,** 457–473, doi:10.1175/JPO2849.1.

——, S. Chen, and P. Hacker, 2007a: Effect of mesoscale eddies on subtropical mode water variability from the Kuroshio Extension System Study (KESS). *J. Phys. Oceanogr.,* **37,** 982–1000, doi:10.1175/JPO3097.1.

——, N. Schnider, and S. Chen, 2007b: Coupled decadal variability in the North Pacific: An observationally constrained idealized model. *J. Climate,* **20,** 3602–3620, doi:10.1175/JCLI4190.1.

Rainville, L., S. R. Jayne, J. L. McClean, and M. E. Maltrud, 2007: Formation of subtropical mode water in a high-resolution ocean simulation of the Kuroshio Extension region. *Ocean Modell.,* **17,** 338–356, doi:10.1016/j.ocemod.2007.03.002.

Rio, M.-H., and F. Hernandez, 2004: A mean dynamic topography computed over the world ocean from altimetry, in situ measurements, and a geoid model. *J. Geophys. Res.,* **109,** C12032, doi:10.1029/2003JC002226.

Suga, T., and K. Hanawa, 1995: The subtropical mode water circulation in the North Pacific. *J. Phys. Oceanogr.,* **25,** 958–970, doi:10.1175/1520-0485(1995)025<0958:TSMWCI>2.0.CO;2.

Taguchi, B., S. Xie, N. Schneider, M. Nonaka, H. Sasaki, and Y. Sasai, 2007: Decadal variability of the Kuroshio Extension: Observations and an eddy-resolving model hindcast. *J. Climate,* **20,** 2357–2377, doi:10.1175/JCLI4142.1.

Talley, L. D., 1988: Potential vorticity distribution in the North Pacific. *J. Phys. Oceanogr.,* **18,** 89–106, doi:10.1175/1520-0485(1988)018<0089:PVDITN>2.0.CO;2.

Teague, W. J., M. J. Carron, and P. J. Hogan, 1990: A comparison between the Generalized Digital Environmental Model and Levitus climatologies. *J. Geophys. Res.,* **95,** 7167–7183, doi:10.1029/JC095iC05p07167.

Tomita, H., S. Kako, M. F. Cronin, and M. Kubota, 2010: Preconditioning of the wintertime mixed layer at the Kuroshio Extension Observatory. *J. Geophys. Res.,* **115,** C12053, doi:10.1029/2010JC006373.

Uehara, H., T. Suga, K. Hanawa, and N. Shikama, 2003: A role of eddies in formation and transport of North Pacific Subtropical Mode Water. *Geophys. Res. Lett.,* **30,** 1705, doi:10.1029/2003GL017542.

Vivier, F., K. A. Kelly, and L. A. Thompson, 1999: Contributions of wind forcing, waves, and surface heating to the sea surface height observations in the Pacific Ocean. *J. Geophys. Res.,* **104,** 20 767–20 788, doi:10.1029/1999JC900096.

——, ——, and ——, 2002: Heat budget in the Kuroshio Extension region: 1993–99. *J. Phys. Oceanogr.,* **32,** 3436–3454, doi:10.1175/1520-0485(2002)032<3436:HBITKE>2.0.CO;2.

Wyrtki, K., 1965: The average annual heat balance of the North Pacific Ocean and its relation to ocean circulation. *J. Geophys. Res.,* **70,** 4547–4559, doi:10.1029/JZ070i018p04547.

Yu, L., R. A. Weller, and B. Sun, 2004: Improving latent and sensible heat flux estimates for the Atlantic Ocean (1988–99) by a synthesis approach. *J. Climate,* **17,** 373–393, doi:10.1175/1520-0442(2004)017<0373:ILASHF>2.0.CO;2.